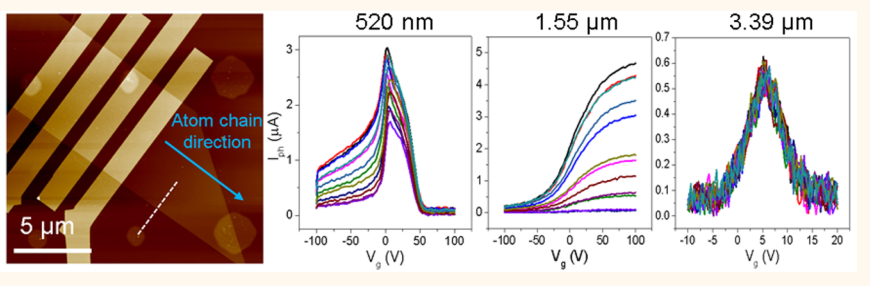


Tellurene Photodetector with High Gain and Wide Bandwidth

Chenfei Shen,^{†,■} Yihang Liu,^{†,■} Jiangbin Wu,^{†,■} Chi Xu,[§] Dingzhou Cui,[‡] Zhen Li,[§] Qingzhou Liu,[‡] Yuanrui Li,[†] Yixiu Wang, Xuan Cao,[‡] Hiroyuki Kumazoe, Fuyuki Shimojo, Aravind Krishnamoorthy,[‡] Rajiv K. Kalia, Aiichiro Nakano, Priya D. Vashishta, Mor R. Amer, Amer, Ahmad N. Abbas, Ahmad N. Abbas, Han Wang, Wenzhuo Wu, Wenzhuo Wu, Ahmad Chongwu Zhou, Theo

Supporting Information



ABSTRACT: Two-dimensional (2D) semiconductors have been extensively explored as a new class of materials with great potential. In particular, black phosphorus (BP) has been considered to be a strong candidate for applications such as high-performance infrared photodetectors. However, the scalability of BP thin film is still a challenge, and its poor stability in the air has hampered the progress of the commercialization of BP devices. Herein, we report the use of hydrothermal-synthesized and air-stable 2D tellurene nanoflakes for broadband and ultrasensitive photodetection. The tellurene nanoflakes show high hole mobilities up to $458 \text{ cm}^2/\text{V} \cdot \text{s}$ at ambient conditions, and the tellurene photodetector presents peak extrinsic responsivity of 383 A/W, 19.2 mA/W, and 18.9 mA/W at 520 nm, $1.55 \mu \text{m}$, and $3.39 \mu \text{m}$ light wavelength, respectively. Because of the photogating effect, high gains up to 1.9×10^3 and 3.15×10^4 are obtained at 520 nm and $3.39 \mu \text{m}$ wavelength, respectively. At the communication wavelength of $1.55 \mu \text{m}$, the tellurene photodetector exhibits an exceptionally high anisotropic behavior, and a large bandwidth of 37 MHz is obtained. The photodetection performance at different wavelength is further supported by the corresponding quantum molecular dynamics (QMD) simulations. Our approach has demonstrated the air-stable tellurene photodetectors that fully cover the short-wave infrared band with ultrafast photoresponse.

KEYWORDS: photodetector, two-dimensional (2D), tellurene, high gain, wide bandwidth, air-stable

ince the discovery of graphene, tremendous efforts have been implemented to study its unique chemical and physical properties. Nevertheless, the zero bandgap of

Received: June 10, 2019
Accepted: December 20, 2019
Published: December 20, 2019



[†]Ming Hsieh Department of Electrical Engineering, [‡]Mork Family Department of Chemical Engineering and Materials Science, [§]Department of Physics, and [#]Collaboratory for Advanced Computing and Simulations, University of Southern California, Los Angeles, California 90089, United States

School of Industrial Engineering, Purdue University, West Lafayette, Indiana 47907, United States

¹Department of Physics, Kumamoto University, Kumamoto 860-8555, Japan

[∇]Center of Excellence for Green Nanotechnologies, Joint Centers of Excellence Program, King Abdulaziz City for Science and Technology, P.O. Box 6086, Riyadh 11442, Saudi Arabia

^ODepartment of Electrical Engineering, University of California, Los Angeles California 90095, United States

Department of Electrical and Computer Engineering, University of Jeddah, 285 Dhahban, Al Sharafeyah, Jeddah 23881, Saudi Arabia

[¶]Department of Electrical and Computer Engineering, King Abdulaziz University, Abdullah Sulayman Street, Jeddah 22254, Saudi Arabia

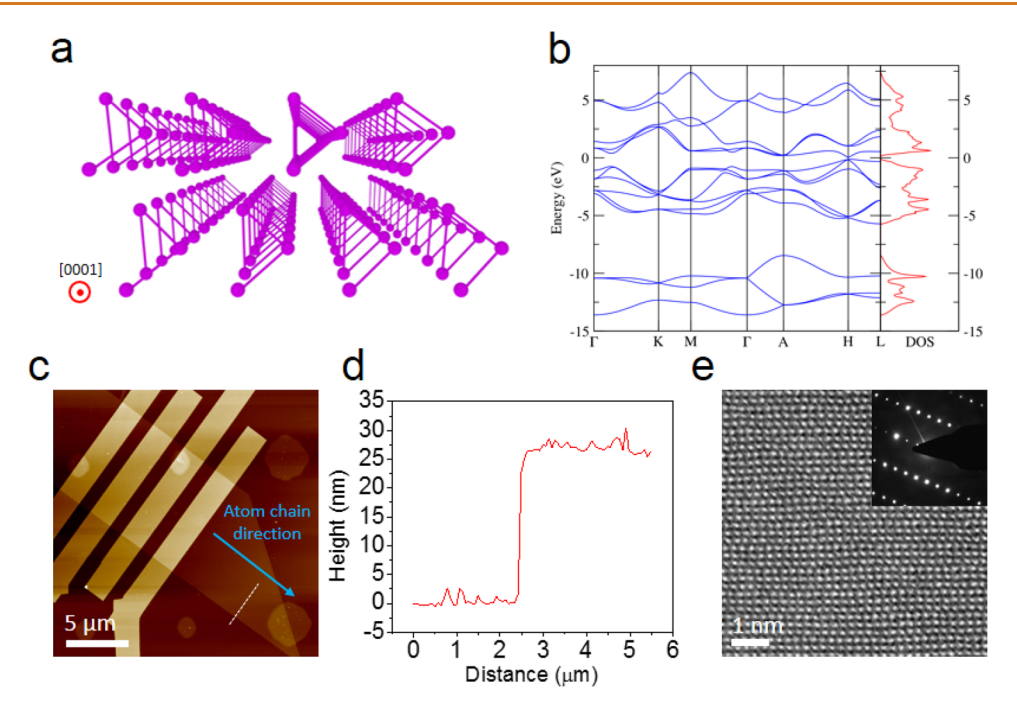


Figure 1. Crystal structure and morphological characterization of tellurene. (a) Schematic illustration of the crystal structure of tellurene. (b) Electronic band structure of tellurene. (Left) Calculated electronic band structure of bulk tellurene along with high symmetry directions in the Brillouin zone. (Right) Calculated electronic density of states. (c) AFM image of back-gate tellurene FET. (d) AFM height profile of the tellurene flake shown in (c), which reveals the thickness of \sim 27 nm. (e) High-resolution TEM image of tellurene. The inset shows the SAED pattern.

graphene greatly limits its applications in electronic and optoelectronic devices. $^{1-3}$ Recently, the elemental two-dimensional (2D) material black phosphorus (BP) with a direct bandgap of \sim 0.3 eV, together with many intriguing properties such as anisotropy and high carrier mobility, has attracted much attention for broadband optoelectronic devices. 4,5 In contrast to the traditional narrow-bandgap semiconductors such as $Hg_{1-x}Cd_xTe$ and InAs, the layered structure of BP makes it a strong candidate for integration with other semiconductor materials and innovative flexible substrates. $^{6-9}$ Unlike the gapless graphene, the suitable and tunable bandgap of BP can effectively suppress the dark current and results in the photodetection with a higher signal-to-noise ratio. $^{10-14}$ However, despite the many merits listed above, the poor ambient stability of BP has significantly limited its application. 15

Recently, low-cost solution synthesis of air-stable 2D tellurene (Te) has been reported by Wu et al. 16 The small bandgap makes tellurene a promising candidate to detect long-wavelength light, while the air stability and low toxicity of tellurene may grant certain advantages over BP and traditional $Hg_{1-x}Cd_xTe$ photodetectors. Herein, we report a study of tellurene photodetectors with a broad operating wavelength range from 520 nm to 3.39 μ m. The bandgap of tellurene was investigated using quantum molecular dynamics (QMD) simulations, which confirmed its suitability for mid-infrared (MIR) photodetector. On this basis, we fabricated field-effect transistors (FETs) using tellurene as the channel material and studied its electrical and optoelectronic properties. The as-fabricated tellurene photodetectors exhibited peak extrinsic responsivity of 383 A/W, 19 mA/W, and 18 mA/W at 520 nm, 1.55 μ m, and 3.39 μ m light wavelength, respectively. High gains up to 1.9×10^3 and $3.15 \times$ 10^4 were obtained at 520 nm and 3.39 μ m wavelength, respectively. A bandwidth of 37 MHz is obtained at 1.55 μ m wavelength, demonstrating the photoconductive effect at this

wavelength. Interestingly, the tellurene photodetectors exhibited exceptionally high anisotropy at 1.55 μ m, which may be due to its intrinsic anisotropic crystal nature. Subsequent investigation of power and frequency dependence associated with the QMD simulations confirmed the photocurrent generation mechanisms in tellurene.

RESULTS AND DISCUSSION

The crystal structure of tellurene is schematically presented in Figure 1a. Each atom in the chain is covalently bonded with its two nearest neighbors, and van der Waals force bundles helical chains together spirally around the [0001] direction (atom chain direction), and thus tellurene can be considered as a 1D or quasi-2D van der Waals solid. The electronic band structure and the density of states of bulk Te has been calculated using density functional theory (DFT) (Figure 1b). 22 Bulk Te is an indirectbandgap semiconductor with a bandgap of 0.17 eV near the H point in the first Brillouin zone. Figure 1c presents the atomic force microscopy (AFM) image of a tellurene field-effect transistor (FET), which shows a piece of as-synthesized tellurene nanoflake with four electrodes. The thickness of the tellurene nanoflake is 27 nm based on the AFM height profile depicted in Figure 1d. The Raman spectrum of the synthesized tellurene nanoflake is exhibited in Figure S1 (Supporting Information). High-resolution transmission electron microscopy (TEM) image of a tellurene flake (Figure 1e) and the inset selected area electron diffraction (SAED) pattern reveal the single-crystalline nature of the tellurene nanoflake. According to the high-resolution TEM image, the interplanar spacings are determined to be 1.9 and 2.8 Å, corresponding to Te (1210) and (0001) planes, respectively. The Raman spectrum of a typical tellurene nanoflake at 532 nm wavelength is exhibited in Figure S1 (Supporting Information).

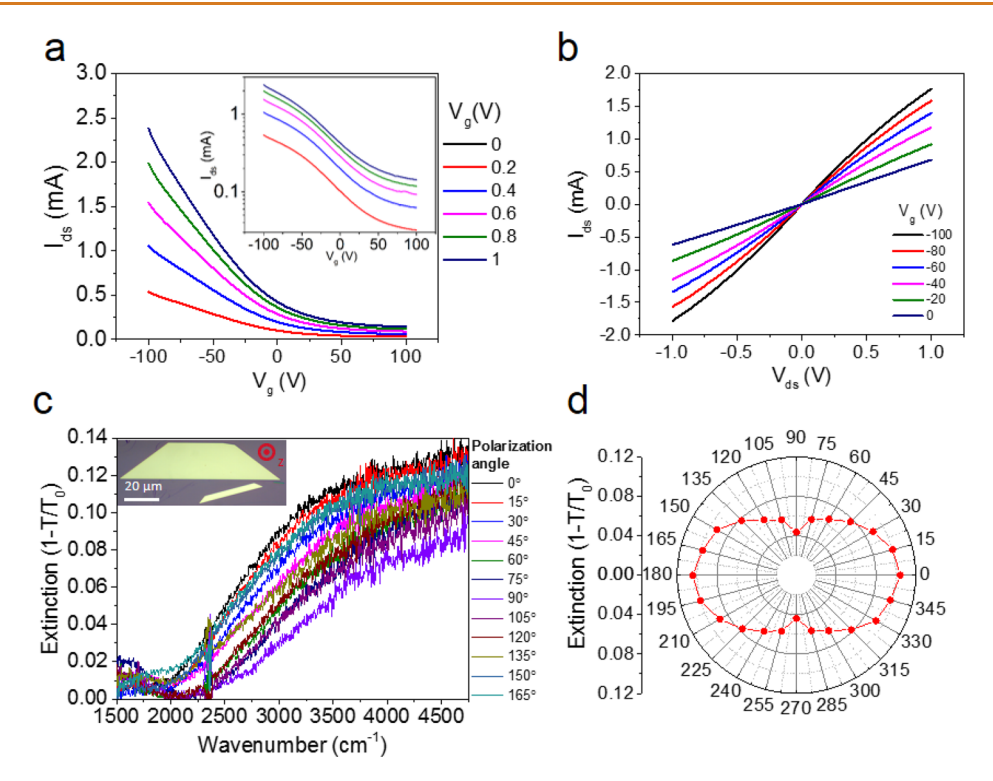


Figure 2. Device performance and infrared extinction characterizations. (a) Transfer curves of a typical tellurene FET. Inset is the transfer curves in the logarithmic scale. (b) $I_{\rm ds}-V_{\rm ds}$ curves of the tellurene FET. (c) Polarization-resolved IR extinction spectra of typical tellurene flake. The inset shows the optical image of the investigated tellurene flake and the 0° reference (z-direction) of the incident light. (d) Dependence of the extinction intensity at 3500 cm⁻¹ with polarization angles.

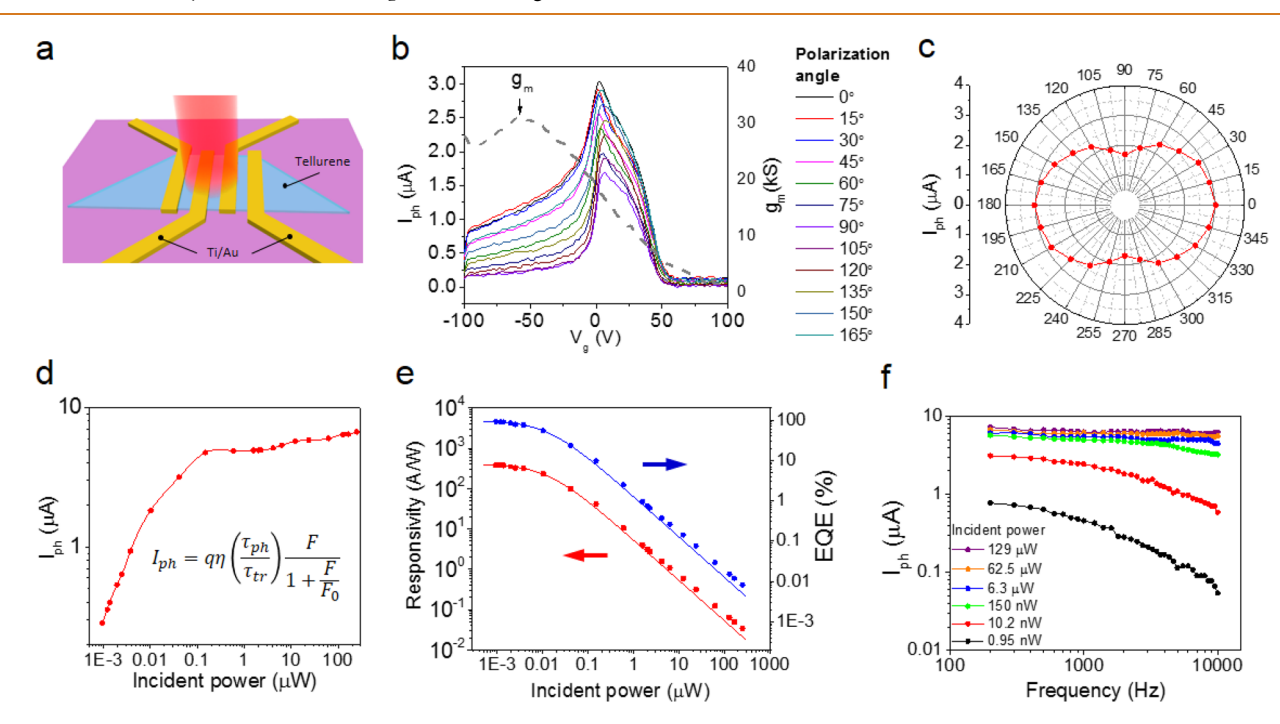


Figure 3. Tellurene photodetector operating at 520 nm. (a) Schematic diagram of the tellurene FET for photodetection. (b) Gate-dependent photocurrent (left axis) and channel trans-conductance ($g_{\rm m}$, dash gray line, right axis) measured at different polarization angles ($V_{\rm ds}=1$ V). (c) Dependence of the photocurrent with polarization angles ($V_{\rm g}=5$ V and $V_{\rm ds}=1$ V). (d) Power dependence of photocurrent ($V_{\rm g}=5$ V and $V_{\rm ds}=1$ V). (e) Power dependence of responsivity and EQE ($V_{\rm g}=5$ V and $V_{\rm ds}=1$ V). (f) Photocurrent versus modulation frequency under various incident powers ($V_{\rm g}=5$ V and $V_{\rm ds}=1$ V).

The tellurene FETs were fabricated on Si/SiO₂ wafer substrates (the thickness of SiO₂ is 300 nm) with vacuum-evaporated Ti/Au (5 nm/50 nm) was used as metal electrode

contacts; the channel length and width were designed to be 1 and 8 μ m, respectively. The electrical properties of the asfabricated tellurene FET are exhibited in Figure 2a,b. The

transfer curves of the FET (Figure 2a) demonstrate a p-type behavior with a hole mobility up to 458 cm²/V·s at room temperature, where the large current under dark condition may because of the relatively large thickness of the tellurene nanoflake (~27 nm). Figure 2c exhibits the polarizationresolved infrared extinction spectra of the nanoflake on the high-resistance Si/SiO₂ wafer substrate (shown in the inserted image), where T_0 and T and are the optical transmission of the bare Si/SiO2 substrate and the tellurene nanoflake on the substrate, respectively; the polarization angles were separated by 15° from the z-direction, and the corresponding extinction spectrum was presented by solid lines with different colors. The measured extinction spectrum of the tellurene nanoflake exhibits an absorption edge at $\sim 2200 \text{ cm}^{-1}$, corresponding to a bandgap of ~0.27 eV, which is comparable to BP and thus reaches the mid-infrared regime. ¹² On the other hand, the polarizationresolved infrared absorption spectra (Figure 2d) presents an anisotropic absorption, indicative of the intrinsically anisotropic nature of the tellurene nanoflake.

In order to exam the photodetection ability of tellurene, the FET-based photodetector was operated at 520 nm, 1.55 μ m, and 3.39 μ m wavelength at ambient condition, where the experimental setup has been presented in the schematic diagram (Figure 3a), and the performance is exhibited in Figure 3 to Figure 5, respectively. At 520 nm wavelength, we first measured the dependence of the photoresponse at $V_{\rm ds}$ = 1 V with different polarization angles separated by 15°, as presented in Figure 3b. All photocurrent (I_{ph}) curves show asymmetric peaks at $V_g = 5 \text{ V}$, which presents a shift of threshold voltage regarding the channel trans-conductance g_m (Figure 3b), indicating the photogating effect in the phtotocurrent generation, and the asymmetry reaches a good agreement with the derivative of FET transfer curves in Figure 2a. Representative transfer curves under dark and 520 nm laser at $V_d = 1$ V were provided in Figure S2. In Figure 3c, the polar plot of the photocurrent dependence with different polarization angles at the optimal condition ($V_g = 5 \text{ V}$ and $V_{ds} = 1 \text{ V}$) is presented. Similar to the IR extinction results in Figure 2d, the photocurrent changed significantly through the rotating of the polarization angles with a dichroic ratio of 1.9 at 520 nm wavelength. The power-dependent photocurrent curves with incident power range from 0.95 nW to 250 μ W are presented in Figure S3a, and the power dependence of the photocurrent at optimal condition is presented in Figure 3d, where the photocurrent increased rapidly and linearly as the incident power increased from 0 to 20 μ W, and then the current showed saturation of $\sim 6 \mu A$ at higher illumination powers. The absolute IR responsivity and the external quantum efficiency (EQE) as a function of incident power at $V_g = 5 \text{ V}$ and $V_{ds} = 1 \text{ V}$ are exhibited in Figure 3e, where the absolute responsivity is defined by the ratio between the photocurrent and the incident laser power. At larger incident power, the decrease of the responsivity clearly demonstrates the photogating effect, and a peak extrinsic responsivity of 383 A/W is measured at the incident power of 1.6 nW. Figure 3f shows the photocurrent under various incident power values, as a function of frequency ranging from 200 to 10k Hz, where the photocurrent data was collected by a lock-in amplifier. When the incident power is as large as 150 nW, 6.3 μ W, 62.5 μ W, or 129 μ W, the photocurrent almost remains constant regardless of the frequency; when the incident power is relatively small, such as 10.2 or 0.95 nW, the photocurrent decreases as the frequency increases due to the decrease of the free carrier density. Compared to the other semiconductor materials with larger bandgap and deeper traps,

the tellurene photodetector shows a much slower photocurrent reduction in the frequency range from 200 Hz to 10 kHz, indicative of the shallow traps in the tellurene nanoflakes. 23

The photocurrent generation mechanism in bare 2D material FET-based photodetector usually is the photoconductive effect, and the photogating effect is an example in particular. 11,24,25 In the case of the photoconductive effect, extra free carriers were generated by photon absorption, and thus the electrical resistance of the semiconductor was reduced. Photoconductive gain (G) can be described as the number of detected charge carriers per single absorbed photon, and it has been widely used in the studies of 2D photoconductor materials. ²⁶ In the equation $G= au_{
m ph}/ au_{
m transit}$, $au_{
m ph}$ is the lifetime of photogenerated carrier and $au_{
m transit}$ is the transit time. In a FET, the $au_{
m transit}=L^2/\mu V_{
m ds}$, where Lis the channel length, μ is the charge carrier mobility, and $V_{\rm ds}$ the drain-source voltage. For photogating effect, holes or electrons are trapped locally so that they can perform field effect as a gate, effectively regulating the resistance of the semiconductor. In this situation, $au_{\rm ph}$ is dominated by the recombination lifetime of the localized trap states, usually leading to a large G^{27-29} . The pure photoconductive effect and photogating effect can be distinguished by comparing the $I_{\rm ds}{-}V_{\rm g}$ and $I_{\rm ph}{-}V_{\rm g}$ curve. When photogating effect is dominant, there is a horizontal shift of $I_{\rm ph}$ V_{σ} trace, due to the existing local gate from localized states. In our case, for the 520 nm wavelength, when the incident power is relatively low, the peak of the $I_{\rm ph}-V_{\rm g}$ curve is at \sim 5 V, which is far away from the maximum of the $I_{ds} - V_g$ curve (at -100 V). This shift indicates the existence of electron-trap centers in tellurene, which would lead to a strong photogating effect. The photogating effect under 520 nm can be confirmed by the sublinear dependence of the photocurrent on laser power (Figure 3d,e) and power-dependent response bandwidth. When the illumination intensity is getting higher, the density of available electron-traps would be decreased, results in a lower responsivity. Upon the filing of electron traps, the increasing of free electron density also raises the electron-hole recombination probability, which can be confirmed by an absorption-ratedependent photocarrier lifetime, $\tau_{\rm ph}(F)$. The relationship between photocurrent and the incident laser power can be depicted by the Hornbeck-Haynes model^{27,30}

$$I_{\rm ph} = q \eta \frac{\tau_{\rm ph}}{\tau_{\rm transit}} \frac{F}{1 + \frac{F}{F}}$$

where q is the elementary electric charge, η is the optical absorption of tellurene channel, F_0 is the photon absorption rate in the trap saturation regime, and F is the absorption rate as expressed below. By using the equation $P = F \cdot hv$, where the product of h and v is the photon energy, we can derive the power-dependent responsivity and EQE

$$R = \frac{I_{\rm ph}}{P} = \frac{q}{hv} \eta \frac{\tau_{\rm ph}}{\tau_{\rm transit}} \frac{1}{1 + \frac{P}{P_{\rm o}}}$$

$$EQE = \frac{R \cdot hv}{q} = \eta \frac{\tau_{ph}}{\tau_{transit}} \frac{1}{1 + \frac{P}{P_{o}}}$$

The two lines in Figure 3e are the fitting results from the above two equations, where $\eta_{\tau_{\rm transit}}^{\tau_{\rm ph}}=971$ and $P_0=13$ nW. If a reasonable absorption rate of 50% is assumed (see Methods), the gain G can be derived to be about 1.9×10^3 , which is slightly lower than the reported gain of BP ($\sim10^4$) at 532 nm

wavelength. ¹¹ Then, due to the high mobility the $\tau_{\rm transit} = L^2/\mu V_{\rm ds} = 140$ ns, which leads to a $\tau_{\rm ph}$ of about 0.27 ms. According to the above equations, a 3-dB bandwidth is calculated as ~600 Hz, which is half of that of BP in the literature (~1.2 kHz). ¹¹ According to equation $f_{3\text{-dB}} = 1/2\pi\tau_{\rm ph}$, the calculated bandwidth still agrees well with the frequency-dependent $I_{\rm ph}$ presented in the high-frequency regime of Figure 3f. Under incident power larger than 10 μ W, the photovoltaic effect dominated the photocurrent generated in the channel, which should be the reason for the higher measured responsivity than the theoretical fitting value.

In Figure 4, the performance of the tellurene photodetectors at 1.55 μ m wavelength was measured at ambient condition, and

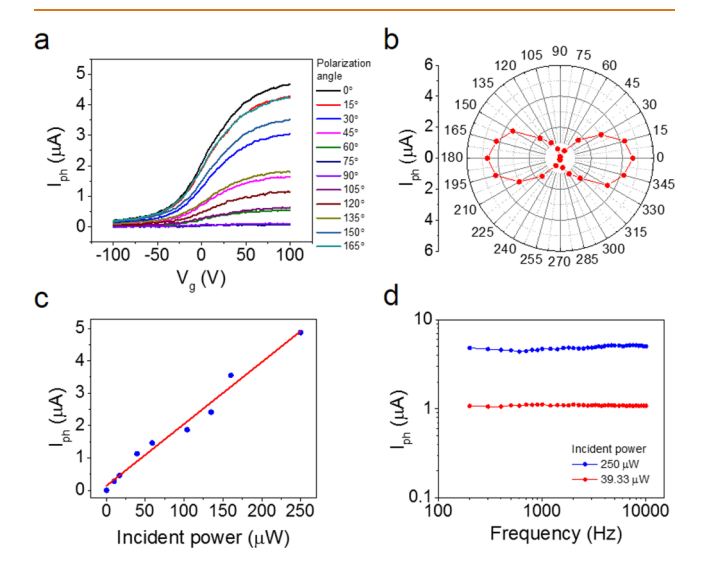


Figure 4. Tellurene photodetector operating at 1.55 μ m. (a) Gate-dependent photocurrent measured at different polarization angles ($V_{\rm ds}=1~{\rm V}$) at 250 μ W incident light power. (b) Dependence of the photocurrent with polarization angles ($V_{\rm g}=100~{\rm V}$ and $V_{\rm ds}=1~{\rm V}$). (c) Power dependence of photocurrent ($V_{\rm g}=100~{\rm V}$ and $V_{\rm ds}=1~{\rm V}$). (d) Photocurrent versus modulation frequency under incident powers of 39.33 and 250 μ W ($V_{\rm g}=100~{\rm V}$ and $V_{\rm ds}=1~{\rm V}$).

the $V_{\rm ds}$ was set to be 1 V. Figure 4a presents the gate-dependent photocurrent measured at different polarization angles. At 1.55 μ m wavelength, because it is very different from the photogating effect no peak is recorded, and the photocurrent increases as the gate voltage increases from -100 V to +100 V. Similar to BP, the monotonic gate voltage dependence of the photocurrent indicates that the photocurrent generation was dominated by the photovoltaic effect.³¹ The polar plot of the photocurrent is presented in Figure 4b, and it is clear that the tellurene photodetector presented a highly anisotropic behavior, which may be due to the intrinsic anisotropic nature of the 2D tellurene crystal structure and will be discussed further in the following sections of this paper. In Figure 4c, the photocurrent varied linearly as the incident light power increased from 0 to 30 μ W with a fitted slope of ~19.2 mA/W, and the power-dependent photocurrent curves with the incident power range from 9.83 to 250 μ W are presented in Figure S3b. Moreover, the photocurrent shows linear dispersion as the incident power increase up to $\sim 250 \,\mu\text{W}$, which also excludes the presence of photogating effect. Figure 4d plots the photocurrent under 39.33 and 250 μ W incident power values versus modulation frequency, and the photocurrent remains almost unchanged as the frequency increased from 200 to 10k Hz, indicating a fast photoresponse due to that the photons with energy higher than the bandgap were absorbed to generate electron—hole pairs. The responsivity is fitted as $\sim\!19.2$ mA/W in Figure 4c, which gives an EQE = $R\!\cdot\!hv/q=1.52\%$. By employing the same absorption coefficient with 520 nm, that is, 50%, the $G=\tau_{\rm ph}/\tau_{\rm transit}$ is reduced as 3.04%, which leads to a very small $\tau_{\rm ph}$ of $\sim\!4.3$ ns. Thus, the 3-dB bandwidth ($f_{3\text{-dB}}$) of 1550 nm is up to 37 MHz, which is far out of the working range of our chopper, as shown in Figure 4d. Therefore, the tellurene photodetector shows extremely fast photoresponse speed under the communication wavelength (1.55 μm).

In Figure 5, we assessed the tellurene photodetectors at the middle-infrared 3.39 μm wavelength at ambient condition, and

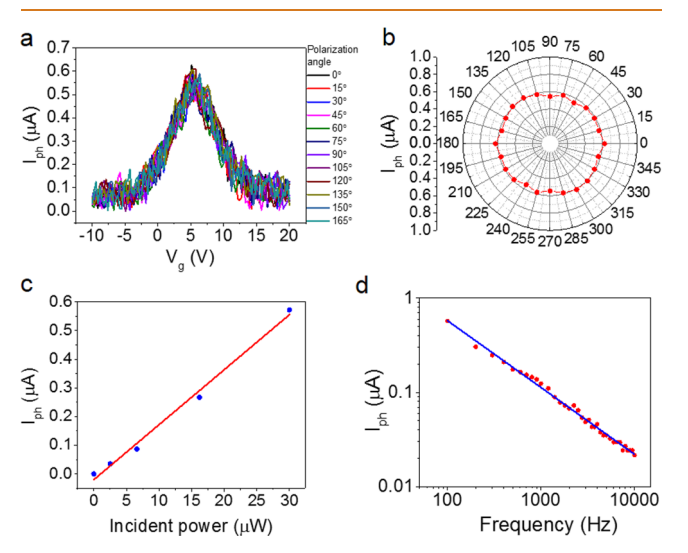


Figure 5. Tellurene photodetector operating at 3.39 μ m. (a) Gate-dependent photocurrent measured at different polarization angles ($V_{\rm ds}=1$ V), at 30 μ W incident light power. (b) Dependence of the photocurrent with polarization angles ($V_{\rm g}=5$ V and $V_{\rm ds}=1$ V). (c) Power dependence of photocurrent ($V_{\rm g}=5$ V and $V_{\rm ds}=1$ V). (d) Photocurrent versus modulation frequency under incident power of 30 μ W ($V_{\rm g}=5$ V and $V_{\rm ds}=1$ V).

the $V_{\rm ds}$ was set as 1 V. The gate-dependent photocurrent measured at different polarization angles is presented in Figure 5a in which all curves show symmetric peaks centered at $V_{o} = 5$ V, showing the pure photogating effect. The polar plot of the photocurrent is exhibited in Figure 5b, in which the tellurene photodetector shows isotropic behavior under the laser of 3.39 um wavelength. In Figure 5c,d, a linear relationship was observed between the photocurrent and the incident power with a fitted slope of ~ 18.9 mA/W, and the photocurrent decreased linearly and rapidly as the frequency increased. By fitting the curve, the $f_{3\text{-dB}}$ is presented at a very low level of \sim 35 Hz, which gives a $\tau_{\rm ph}$ of 4.5 ms. Thus, a very high G can be presented as $\sim 3.15 \times 10^4$, which is the evidence of the photogating effect and much higher than that at 520 nm. On the other hand, the responsivity is 18.9 mA/W under this wavelength, which leads to a very low EQE of 0.66%, regarding the high gain. As discussed above, the absorption coefficient η = EQE/ $G = 2.1 \times 10^{-7}$. The weak absorption at this wavelength is because it is close to the absorption edge of the indirect bandgap, which is confirmed by the DFT calculation in Figure 1b. The power-dependent photocurrent curves with the incident power range from 2.5 to 30 μ W are presented in Figure S3c. In contrast to the reported data of BP photoresponse at 3.39 μ m

wavelength, the tellurene photodetector shows lower responsivity but higher 3-dB cutoff frequency due to the very shallow traps in tellurene nanoflakes. Although the photocurrent is relatively small at 3.39 μ m wavelength without any anisotropic behavior, we have demonstrated the photoresponse of 2D tellurene fully covering the short-wave infrared band.

The hydrothermal synthesized tellurene nanoflakes should contain a considerable amount of vacancy defects. In order to elucidate how vacancy can affect the photocurrent generation in tellurene, we simulated the optical absorption spectra with and without vacancy through QMD simulation, as presented by the dimensionless oscillator strength versus photon energy in Figure 6a,b, respectively. Figure 6a shows the simulation without

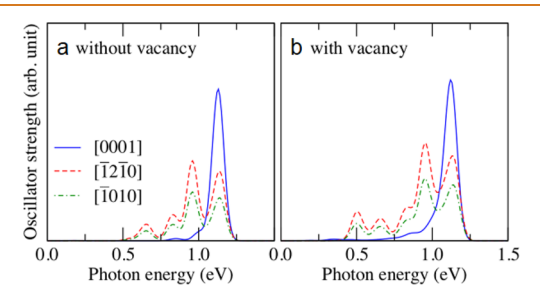


Figure 6. Simulated optical absorption spectra represented as folded oscillator strengths without (a) and with (b) vacancy for the [0001] (blue solid line), $[\overline{1}2\overline{1}0]$ (red dash line), and $[\overline{1}010]$ (green dash line) directions.

vacancy, and the absorption band is ranged from 0.5 to 1.25 eV. The absorption spectra along $\lceil \overline{1210} \rceil$ and $\lceil \overline{1010} \rceil$ directions have four peaks at 0.63, 0.81, 0.95, and 1.12 eV, while at 1.2 eV photon energy the absorption along [0001] direction is much stronger than that along with the other two directions. Similar to the simulation with vacancy defects shown in Figure 6b, the vacancy in tellurene can extend the photoexcitation bandwidth to as low as 0.25 eV but with relatively low oscillator strength, which can explain the small photocurrent (due to the weak absorption, i.e., oscillator strength) and very high gain due to the strong photogating effect (caused by large amount of defects) at 3.39 μ m and the isotropy in the gate-dependent photocurrent measurement. Moreover, in both simulation figures the absorption intensity at 0.8 eV does not show a large difference, indicating that the vacancy defects may only have very limited effects on the anisotropy at 1.55 μ m wavelength, and thus the highly anisotropic behavior in Figure 4b should come from the intrinsic anisotropic structure of tellurene nanoflakes, and photogating effect should be very weak at this wavelength, as presented above. On the basis of our observation above, the tellurene photodetector presents the photogating effect at 520 nm and 3.39 μ m, which should due to the small amount of the photocarriers. However, at 1.55 μ m wavelength, the photodetector shows a different working mechanism of photovoltaic, which may due to the limitation of our current optical experimental setup. The smallest incident power can be obtained is 9.83 μ W at 1.55 μ m, which is much larger than that of 520 nm. Moreover, according to the absorption spectra presented in Figure 6, the absorption at 1.55 μ m is much stronger than that of 520 nm and 3.39 μ m wavelength, and thus the number of photocarriers should be much higher than the density of trap states, leading to the strong photovoltaic effect.

CONCLUSION

In summary, a highly sensitive mid-infrared photodetector based on 2D tellurene has been demonstrated. The FET-based tellurene photodetector exhibits peak extrinsic responsivity of 383 A/W, 19 mA/W, and 18 mA/W at 520 nm, 1.55 μ m, and 3.39 μ m wavelength, respectively, showing the detection ability fully captures the short-wave infrared band, even down to the mid-infrared range. Under the wavelength of 520 nm and 3.39 μ m, the gains are up to 1.9×10^3 and 3.15×10^4 , respectively, due to the photogating effect. At the communication wavelength $(1.55 \mu m)$, a relatively large bandwidth (37 MHz) is obtained, which is the credit of pure photoconductive effect in this range. Our study indicates that tellurene could be an excellent candidate for high-performance and ultrafast photodetectors. The distinctive polarization sensitivity, ultrafast responsivity, wide detection range, and the solution-process-enabled easiness of integration with a variety of materials make tellurene an encouraging 2D semiconductor for the mid-infrared photodetection. We believe the air-stable properties and the facile synthesis of tellurene should stimulate broad interests in the fields of nanophotonics, thermoelectronics, and piezoelectronics, and there is still much work left to be done on tellurene, such as the large-area thin-film synthesis and more fundamental studies based on its unique crystal structure.

METHODS

Tellurene Flake Synthesis. Tellurene was synthesized by a hydrothermal method. Na_2TeO_3 and PVP were used as the precursors. The precursors were dissolved into deionized water and transferred into a Teflon-lined stainless-steel autoclave, and an ammonia solution and hydrazine hydrate were filled into the autoclave. The autoclave was heated to 180 °C with a heating rate of 5 °C/min and maintained at 180 °C for 10 h. After the cooling down process, the resulted solution was precipitated by centrifugation at 5000 rpm for 5 min, and the final product was washed with deionized water at least three times.

Material Characterizations. An AFM, DI 3100 Digital Instruments, was used to scan the tellurene-based FETs to characterize the thickness of the nanoflake and the channel lengths of the FETs. The resolution of the AFM images is 512×512 . Raman spectra were performed with a Raman spectrometer (Renishaw), and a 532 nm excitation laser with a laser spot size of $\sim 1~\mu m$ was used in the experiments. A field-emission transmission electron microscopy (JEOL JEM 2100F) was used to perform the TEM experiments.

Tellurene Photodetector Device Fabrication. The tellurene flakes were transferred onto $\mathrm{Si/SiO_2}$ (the thickness of the $\mathrm{SiO_2}$ layer is 300 nm) substrates with alignment markers. A bilayer poly(methyl methacrylate) (PMMA A6 and PMMA A2) was then spin-coated onto the $\mathrm{Si/SiO_2}$ surface. Electron-beam lithography was performed to pattern the drain and source electrodes, followed by standard development, metal deposition, and lift-off processes. Ti (5 nm) and Au (50 nm) electrodes were deposited under the pressure of 9×10^{-7} Torr with an e-beam evaporator.

FET and Photodetector Measurements. The FET transfer curves and $I_{\rm ds}$ – $V_{\rm ds}$ family curves were measured using a semiconductor analyzer (Agilent 4156B) with a probe station at ambient conditions. First, a green laser beam (520 nm) was focused on the photodetector channel, and a spot with a size of ~3.5 μ m was obtained to cover the channel area, and a half-wave plate was used to control the incident light polarization. According to the previous experimental result, the absorption was estimated to be 50% on a ~30 nm-thick tellurene nanoflake in the α -direction at 520 nm wavelength (2.38 eV). For tellurene nanoflake thicker than 10 nm, a constant absorption coefficient α (cm⁻¹) was assumed. For near IR laser at 1.550 μ m, the spot size was estimated to be ~5 μ m. For the experiments at 3.39 μ m wavelength, a helium—neon laser was used and integrated into a Fourier transform infrared spectrometer (FTIR) system. The laser beam was

focused to a spot by using a ZnSe objective with a microscope system, and a ZnSe holographic wire grid polarizer was used to adjust the polarization direction of the incident light. Multiple neutral density filters were used to tune the power of the incident light. For the measurement of the photocurrent, a lock-in amplifier was used to acquire experimental data, where 1 s, a much longer time than the time constant of laser modulation time at 200 Hz frequency (5 ms), was chosen as the integration time. In the lock-in setup, the peak-to-peak values used in this study were converted by the root-mean-square values of the photocurrent.

Simulation. Quantum molecular dynamics (QMD) simulations were performed by the trajectory following of Te atoms and the quantum mechanical computing of interatomic forces from first principles.^{32,33} In our QMD simulations, the projector augmentedwave method was used to compute the quantum states.³⁴ Projector functions were initialized for the 5s and 5p states of tellurium. With the help of density functional theory (DFT), 35,36 the exchange-correlation energy can be calculated by the generalized gradient approximation.³⁸ For tellurene, van der Waals correction was introduced with the DFT-D method.³⁹ The electronic pseudowave functions and pseudocharge density were expanded by plane waves with cutoff energies of 10 and 100 Ry, respectively. Oscillator strength was simulated using the linearresponse time-dependent DFT.³⁷ Simulations were conducted on a supercell structure consisting of $6 \times 6 \times 6$ unit cells. In the calculation of the electronic band structure, the Γ -point was employed for Brillouinzone sampling. The electronic band structure and density of states of the bulk β -Te structure were calculated on a periodic unit cell, where the reciprocal space was sampled using a dense $36 \times 36 \times 36$ k-point mesh. The QMD simulation was realized with massively parallel computering.

ASSOCIATED CONTENT

Supporting Information

The Supporting Information is available free of charge at https://pubs.acs.org/doi/10.1021/acsnano.9b04507.

Details of the Raman spectrum of a typical tellurene flake at 532 nm wavelength, and gate-dependent photocurrent measured at different incident power under 520 nm, 1.55 μ m, and 3.39 μ m laser (PDF)

AUTHOR INFORMATION

Corresponding Authors

*E-mail: chongwuz@usc.edu (C.Z.).

*E-mail: han.wang.4@usc.edu (H.W.).

*E-mail: wenzhuowu@purdue.edu (W.W.).

*E-mail: ahmad.nabil.abbas@gmail.com (A.N.A.).

ORCID 🌕

Yihang Liu: 0000-0002-2491-9439

Aravind Krishnamoorthy: 0000-0001-6778-2471

Aiichiro Nakano: 0000-0003-3228-3896 Priya D. Vashishta: 0000-0003-4683-429X Mor R. Amer: 0000-0003-3318-2667

Han Wang: 0000-0001-5121-3362 Wenzhuo Wu: 0000-0003-0362-6650 Chongwu Zhou: 0000-0001-8448-8450

Author Contributions

C.S., Y.L., and J.W. contributed equally to this work.

Notes

The authors declare no competing financial interest.

ACKNOWLEDGMENTS

We would like to acknowledge the collaboration of this research with King Abdul-Aziz City for Science and Technology (KACST) via The Center of Excellence for Nanotechnologies (CEGN). We acknowledge the funding support from the University of Southern California. A portion of the images and data used in this article were acquired at The Center for Electron Microscopy and Microanalysis, University of Southern California. The simulation work was supported as part of the Computational Materials Sciences Program funded by the U.S. Department of Energy, Office of Science, Basic Energy Sciences, under Award Number DE-SC0014607. The simulations were performed at the Argonne Leadership Computing Facility under the DOE INCITE program and at the Center for High Performance Computing of the University of Southern California. The synthesis of tellurene materials is supported by the National Science Foundation under Grant CMMI-1762698.

REFERENCES

- (1) Novoselov, K. S.; Mishchenko, A.; Carvalho, A.; Castro Neto, A. H. 2D Materials and van der Waals Heterostructures. *Science* **2016**, 353, aac9439.
- (2) Allen, M. J.; Tung, V. C.; Kaner, R. B. Honeycomb Carbon: A Review of Graphene. *Chem. Rev.* **2010**, *110*, 132–145.
- (3) Tan, C.; Cao, X.; Wu, X.-J.; He, Q.; Yang, J.; Zhang, X.; Chen, J.; Zhao, W.; Han, S.; Nam, G.-H.; Sindoro, M.; Zhang, H. Recent Advances in Ultrathin Two-Dimensional Materials. *Chem. Rev.* **2017**, *117*, 6225–6331.
- (4) Li, L.; Yu, Y.; Ye, G. J.; Ge, Q.; Ou, X.; Wu, H.; Feng, D.; Chen, X. H.; Zhang, Y. Black Phosphorus Field-Effect Transistors. *Nat. Nanotechnol.* **2014**, *9*, 372–377.
- (5) Liu, H.; Neal, A. T.; Zhu, Z.; Luo, Z.; Xu, X.; Tomanek, D.; Ye, P. D. Phosphorene: An Unexplored 2D Semiconductor with a High Hole Mobility. *ACS Nano* **2014**, *8*, 4033–4041.
- (6) Liu, H.; Du, Y.; Deng, Y.; Ye, P. D. Semiconducting Black Phosphorus: Synthesis, Transport Properties and Electronic Applications. *Chem. Soc. Rev.* **2015**, *44*, 2732–2743.
- (7) Zhu, W.; Park, S.; Yogeesh, M. N.; McNicholas, K. M.; Bank, S. R.; Akinwande, D. Black Phosphorus Flexible Thin Film Transistors at Gighertz Frequencies. *Nano Lett.* **2016**, *16*, 2301–2306.
- (8) Buscema, M.; Groenendijk, D. J.; Blanter, S. I.; Steele, G. A.; Van Der Zant, H. S.; Castellanos-Gomez, A. Fast and Broadband Photoresponse of Few-Layer Black Phosphorus Field-Effect Transistors. *Nano Lett.* **2014**, *14*, 3347–3352.
- (9) Rogalski, A. HgCdTe Infrared Detector Material: History, Status and Outlook. *Rep. Prog. Phys.* **2005**, *68*, 2267–2336.
- (10) Ye, Z.; Campbell, J. C.; Chen, Z.; Kim, E.-T.; Madhukar, A. Noise and Photoconductive Gain in InAs Quantum-Dot Infrared Photodetectors. *Appl. Phys. Lett.* **2003**, *83*, 1234–1236.
- (11) Guo, Q.; Pospischil, A.; Bhuiyan, M.; Jiang, H.; Tian, H.; Farmer, D.; Deng, B.; Li, C.; Han, S.-J.; Wang, H.; Xia, X.; Ma, T.-P.; Mueller, T.; Xia, F. Black Phosphorus Mid-Infrared Photodetectors with High Gain. *Nano Lett.* **2016**, *16*, 4648–4655.
- (12) Ling, X.; Wang, H.; Huang, S.; Xia, F.; Dresselhaus, M. S. The Renaissance of Black Phosphorus. *Proc. Natl. Acad. Sci. U. S. A.* **2015**, 112, 4523–4530.
- (13) Wang, X.; Jones, A. M.; Seyler, K. L.; Tran, V.; Jia, Y.; Zhao, H.; Wang, H.; Yang, L.; Xu, X.; Xia, F. Highly Anisotropic and Robust Excitons in Monolayer Black Phosphorus. *Nat. Nanotechnol.* **2015**, *10*, 517–521.
- (14) Yuan, H.; Liu, X.; Afshinmanesh, F.; Li, W.; Xu, G.; Sun, J.; Lian, B.; Curto, A. G.; Ye, G.; Hikita, Y.; et al. Polarization-Sensitive Broadband Photodetector Using a Black Phosphorus Vertical *p-n* Junction. *Nat. Nanotechnol.* **2015**, *10*, 707–713.
- (15) Wood, J. D.; Wells, S. A.; Jariwala, D.; Chen, K.-S.; Cho, E.; Sangwan, V. K.; Liu, X.; Lauhon, L. J.; Marks, T. J.; Hersam, M. C. Effective Passivation of Exfoliated Black Phosphorus Transistors against Ambient Degradation. *Nano Lett.* **2014**, *14*, 6964–6970.
- (16) Wang, Y.; Qiu, G.; Wang, R.; Huang, S.; Wang, Q.; Liu, Y.; Du, Y.; Goddard, W. A.; Kim, M. J.; Xu, X.; Ye, P. D.; Wu, W. Field-Effect

Transistors Made from Solution-Grown Two-Dimensional Tellurene. *Nat. Electron.* **2018**, *1*, 228–236.

- (17) Wu, W.; Qiu, G.; Wang, Y.; Wang, R.; Ye, P. Tellurene: Its Physical Properties, Scalable Nanomanufacturing, and Device Applications. *Chem. Soc. Rev.* **2018**, *47*, 7203–7212.
- (18) Amani, M.; Tan, C.; Zhang, G.; Zhao, C.; Bullock, J.; Song, X.; Kim, H.; Shrestha, V. R.; Gao, Y.; Crozier, K. B.; Scott, M.; Javey, A. Solution-Synthesized High-Mobility Tellurium Nanoflakes for Short-Wave Infrared Photodetectors. *ACS Nano* **2018**, *12*, 7253–7263.
- (19) Xia, F.; Wang, H.; Jia, Y. Rediscovering Black Phosphorus as an Anisotropic Layered Material for Optoelectronics and Electronics. *Nat. Commun.* **2014**, *5*, 4458.
- (20) Amani, M.; Regan, E.; Bullock, J.; Ahn, G. H.; Javey, A. Mid-Wave Infrared Photoconductors Based on Black Phosphorous-Arsenic Alloys. *ACS Nano* **2017**, *11*, 11724–11731.
- (21) Liu, B.; Köpf, M.; Abbas, A. N.; Wang, X.; Guo, Q.; Jia, Y.; Xia, F.; Weihrich, R.; Bachhuber, F.; Pielnhofer, F.; Wang, H.; Dhall, R.; Cronin, S. B.; Ge, M.; Fang, X.; Nilges, T.; Zhou, C. Black Arsenic-Phosphorus: Layered Anisotropic Infrared Semiconductors with Highly Tunable Compositions and Properties. *Adv. Mater.* **2015**, *27*, 4423–4329.
- (22) Apte, A.; Bianco, E.; Krishnamoorthy, A.; Yazdi, S.; Rao, R.; Glavin, N.; Kumazoe, H.; Varshney, V.; Roy, A.; Shimojo, F.; Ringe, E.; Kalia, R. K.; Nakano, A.; Tiwari, C. S.; Vashishta, P.; Kochat, V.; Ajayan, P. M. Polytypism in Ultrathin Tellurium. 2D Mater. 2019, 6 (6), No. 015013.
- (23) Wang, W.; Klots, A.; Prasai, D.; Yang, Y.; Bolotin, K. I.; Valentine, J. Hot Electron-Based Near-Infrared Photodetection Using Bilayer MoS₂. *Nano Lett.* **2015**, *15*, 7440–7444.
- (24) Buscema, M.; Island, J. O.; Groenendijk, D. J.; Blanter, S. I.; Steele, G. A.; Zant, H. S. J. v. d.; Castellanos-Gomez, A. Photocurrent Generation with Two-Dimensional van der Waals Semiconductors. *Chem. Soc. Rev.* **2015**, *44*, 3691–3718.
- (25) Fang, H.; Hu, W. Photogating in Low Dimensional Photodetectors. *Adv. Sci.* **2017**, *4*, 1700323.
- (26) Neamen, D. A. Semiconductor Physics and Devices: Basic Principles, 4th ed.; McGraw-Hill: New York, 2011.
- (27) Soci, C.; Zhang, A.; Xiang, B.; Dayeh, S. A.; Aplin, D. P. R.; Park, J.; Bao, X. Y.; Lo, H.; Wang, D. ZnO Nanowire UV Photodetectors with High Internal Gain. *Nano Lett.* **2007**, *7*, 1003–1009.
- (28) Koppens, F. H. L.; Mueller, T.; Avouris, Ph.; Ferrari, A. C.; Vitiello, M. S.; Polini, M. Photodetectors Based on Graphene, Other Two-Dimensional Materials and Hybrid Systems. *Nat. Nanotechnol.* **2014**, *9*, 780–793.
- (29) Roy, K.; Padmanabhan, M.; Goswami, S.; Phanindra Sai, T.; Ramalingam, G.; Raghavan, S.; Ghosh, A. Graphene–MoS₂ Hybrid Structures for Multifunctional Photoresponsive Memory Devices. *Nat. Nanotechnol.* **2013**, *8*, 826–830.
- (30) Low, T.; Engel, M.; Steiner, M.; Avouris, P. Origin of Photoresponse in Black Phosphorus Phototransistors. *Phys. Rev. B: Condens. Matter Mater. Phys.* **2014**, 90, No. 081408.
- (31) Hong, T.; Chamlagain, B.; Lin, W.; Chuang, H. J.; Pan, M.; Zhou, Z.; Xu, Y.-Q. Polarized Photocurrent Response in Black Phosphorus Field-Effect Transistors. *Nanoscale* **2014**, *6*, 8978–8983.
- (32) Car, R.; Parrinello, M. Unified Approach for Molecular Dynamics and Density-Functional Theory. *Phys. Rev. Lett.* **1985**, *55*, 2471–2474.
- (33) Payne, M. C.; Teter, M. P.; Allan, D. C.; Arias, T. A.; Joannopoulos, J. D. Iterative Minimization Techniques for *Ab Initio* Total-Energy Calculations: Molecular Dynamics and Conjugate Gradients. *Rev. Mod. Phys.* **1992**, *64*, 1045–1097.
- (34) Blochl, P. E. Projector Augmented-Wave Method. *Phys. Rev. B: Condens. Matter Mater. Phys.* **1994**, *50*, 17953–17979.
- (35) Hohenberg, P.; Kohn, W. Inhomogeneous Electron Gas. *Phys. Rev.* **1964**, *136*, B864–B871.
- (36) Kohn, W.; Sham, L. Self-Consistent Equations Including Exchange and Correlation Effects. *Phys. Rev.* **1965**, *140*, A1133–A1138. (37) Perdew, J. P.; Burke, K.; Ernzerhof, M. Generalized Gradient Approximation Made Simple. *Phys. Rev. Lett.* **1996**, *77*, 3865–3868.

- (38) Grimme, S. Semiempirical GGA-Type Density Functional Constructed with a Long-Range Dispersion Correction. *J. Comput. Chem.* **2006**, 27, 1787–1799.
- (39) Casida, M. E.; Huix-Rotllant, M. Many-Body Perturbation Theory (MBPT) and Time-Dependent Density-Functional Theory (TD-DFT): MBPT Insights About What Is Missing In, and Corrections To, the TD-DFT Adiabatic Approximation. In Density-Functional Methods for Excited States. *Top. Curr. Chem.* **2015**, 368, 1–60.
- (40) Shimojo, F.; Kalia, R. K.; Kunaseth, M.; Nakano, A.; Nomura, K.; Ohmura, S.; Shimamura, K.; Vashishta, P. A Divide-Conquer-Recombine Algorithmic Paradigm for Large Spatiotemporal Quantum Molecular Dynamics Simulations. *J. Chem. Phys.* **2014**, *140*, 18A529.